Flow-energy harvesting using a fully passive flapping foil: A guideline on design and operation

Fuwang Zhao[a,b], M.N. Mumtaz Qadri[a,c], Zhaokun Wang[a] and Hui Tang[a,b,*]

[a]*Research Center for Fluid-Structure Interactions, Department of Mechanical Engineering, The Hong Kong Polytechnic University, Kowloon, Hong Kong, China*

[b]*The Hong Kong Polytechnic University Shenzhen Research Institute, Shenzhen 518057, China*

[c]*Department of Aerospace Engineering, College of Aeronautical Engineering, National University of Sciences and Technology, Risalpur, Pakistan*

ARTICLE INFO

ABSTRACT

Following our previous work [Int. J. Mech. Sci. (2020), vol. 177, 105587], we searched the best power extraction performance of a novel flow-energy harvester, which utilizes a fully passive flapping foil to extract energy from air/water flows. A series of water-tunnel experiments were conducted on the same test model at the Reynolds number around 10^5. Through investigating the effects of two unexplored key parameters, a higher overall maximum power conversion efficiency of 42.7% was obtained at water speed 0.71 m/s and foil pitching amplitude 60°, corresponding to a larger mean power output of about 1.51 W. A quasi-steady theoretical model was also developed to fast predict the system performance in a larger parameter space. It was found that, in addition to typical dynamics, i.e., a flapping cycle includes two pure-heaving phases and two stroke-reversal phases, the foil system can also continuously operate in a "no-pure-heaving" zone where a flapping cycle only includes two successive stroke-reversal phases. Through these experimental and theoretical studies, a useful guideline was proposed on the design and operation of the foil system.

1. Introduction

For decades people have been exploring reliable renewable energy from wind, river and ocean. Rotary turbines have been widely used due to their high energy conversion efficiencies. Besides this classical, mature technology, novel technologies also emerged from time to time. For example, a concept that can extract flow energy using flapping foils was proposed, earliest by McKinney and DeLaurier (1981). Compared with conventional rotary turbines, this concept is centrifugal stress free and hence is structurally more robust. It is also environmentally friendly due to the relatively low tip speeds, thus reducing the impact on flying/aquatic animals. Furthermore, it can be deployed in wide and shallow water flows due to its rectangular sweep area (Xiao and Zhu, 2014).

In general, flapping-foil based flow-energy harvesters can operate in three different modes: the *fully active* mode where both the heaving and pitching motions are prescribed (e.g., Xiao, Liao, Yang and Peng, 2012; Kim, Strom, Mandre and Breuer, 2017), the *semi-active* or *semi-passive* mode where one of the motions is prescribed while the other is induced by the flow (e.g., Liu, Qu and Shi, 2020), and the *fully passive* mode where both the motions are flow-induced. Extensive studies have been conducted on fully active and semi-active systems, but only a limited number of studies were focused on fully passive systems (Young, Lai and Platzer, 2014). Compared with systems operating in the other two modes, fully passive systems do not involve any actuator, which simplifies the structure and reduces maintenance costs.

According to the actual realization, flapping-foil based flow-energy harvesters operating in the fully passive mode can be further classified into four types, as summarized in Table 1. In the first type, a mechanical linkage is implemented to interconnect the foil's heaving motion and pitching motion, such that the system has only a single degree-of-freedom (DOF), and there is a fixed phase difference between these two motions. McKinney and DeLaurier (1981) adopted a Scotch-yoke mechanism in the very first Type I system called *wingmill*. Through theoretical and experimental investigations, they achieved the maximum power extraction efficiency of 28.3% using a NACA0012 foil operating at the Reynolds number about $Re = 10^5$ and with the pivot axis located at mid chord, pitching amplitude set as 30° and

*Corresponding author

✉ h.tang@polyu.edu.hk (H. Tang)

ORCID(s): 0000-0002-6774-507X (H. Tang)

Table 1
Summary of studies on fully passive flapping-foil based flow-energy harvesters

Type	Authors (Year)	Method	Foil Type	x_p/c	Re (×10^4)	$\overline{C}_{p,max}$	η_{max}[a]
	McKinney & DeLaurier (1981)	Exp	NACA0012	0.5	8.5~11	0.17	28.3%
I	Jones et al. (1999)	Exp & CFD	NACA0012	0.5	1.86~3.1	0.4	26%
	Young et al. (2013)	CFD	NACA0012	0.5	0.11~210	-	41%
	Jones et al. (2003)	Exp	NACA0014	0.25	2.2	0.25	10%
	Kinsey et al. (2011)	Exp & CFD	NACA0015	0.33	28.8~50.4	-	30% (2 foils)
II	Kinsey et al. (2012a)	CFD	NACA0015	0.33	43.1~50	0.976	60% (2 foils)
	Kinsey et al. (2012b)	CFD	NACA0015	0.33	50	-	64% (2 foils)
	Xu et al. (2019)	Exp & CFD	NACA0018	0.33	10~12	-	37% (2 foils)
	Peng & Zhu (2009)	CFD	NACA0015	0~1.0	-	-	20%
	Zhu (2011)	CFD	NACA0015	0.33	0.01~0.1	-	30%
	Veilleux & Dumas (2017)	CFD	NACA0015	0.17	50	1.079	34%
III	Boudreau et al. (2018)	Exp	NACA0015	0.33	2.1	0.86	31%
	Duarte et al. (2019)	Exp	NACA0015	0~1.0	6	-	-
	Boudreau et al. (2020)	CFD	NACA0015	0.25	390	2.0	53.8%
	Jiang et al. (2019, 2020)	CFD	C-shape	0.5	-	1.34	40%
	Wang et al. (2020)	CFD	NACA0012	0~1.0	0.04	-	-
IV	Platzer el al. (2009)	Exp	Flat	0.2~0.8	-	-	32%
	Mumtaz Qadri et al. (2020)	Exp	Flat	0.6~0.8	6.4~9.7	0.43	30.7%(35.2%)

[a] All evaluated using the foil's largest distance swept by the leading/trailing edge, except the value shown in the parentheses of the last item, which was evaluated using the swept distance of the pivot axis.

phase difference fixed at 90°. Jones, Davids and Platzer (1999) developed another Type I system using a pair of swing arms and a pair of pitch arms, which was able to operate in water flow of speed as low as 0.3 m/s. Young, Ashraf, Lai and Platzer (2013) further investigated this system using numerical simulations. It was found that, when the foil pitches sinusoidally, the efficiency is about 30%, whereas it can exceed 41% when the foil pitches non-sinusoidally.

In the second type, two or more foils in tandem configuration are adopted, which are interconnected with a fixed, non-zero phase difference such that the null spot of one foil coincides with the power stroke of the other achieving continuous flapping motions. Systems of this type also have only a single DOF. Jones, Lindsey and Platzer (2003) extended their Type I system to a Type II system and achieved smoother flapping motion by operating the two foils with a distance of 9.6c (c is the chord of the foil) and a phase difference of 90°. Kinsey, Dumas, Lalande, Ruel, Mehut, Viarouge, Lemay and Jean (2011) designed another Type II system, in which the two foils' distance and phase difference were fixed at 5.4c and 180°, respectively. They tested this system by mounting it on a specially designed pontoon boat. Compared to the maximum power extraction efficiency of 20% for the single-foil system, this system can attain the maximum total efficiency of 30%. Kinsey and Dumas (2012a,b) further conducted a series of numerical investigations on this system, and identified a new parameter "global phase shift", a combination of the flow speed, flapping period, foil distance and phase difference, which can well predict the system's optimum conditions. They pointed out that this parameter can be more reliable when the two foils share the same flapping frequency and amplitude. In addition, they also found that the low-pressure region in the wake of the upstream foil can help enhance the lift of the downstream foil and hence improve the overall system performance. This observation was further supported by Xu, Xu, Duan, Song and Lei (2019) in their experimental and numerical studies on a Type II system.

In the third type, a single foil is connected with a torsional spring and a linear spring, passively oscillating in two DOF. Flapping of this foil is a classic aeroelastic phenomenon, i.e., wing flutter, which has been studied intensively in the aeroelasticity community. However, most of existing studies were focused on how to mitigate the flutter instability, and only a few looked at the energy extraction by utilizing this instability. Peng and Zhu (2009), Zhu (2011), Veilleux and Dumas (2017), Jiang, Wang, Zhang and Xie (2019, 2020), and Wang, Du, Zhao, Thompson and Sun (2020)

conducted a series of numerical studies to investigate the influences of natural frequency, pivot location, spring stiffness, damping, and 3D effects on the system's energy extraction performance. Some experimental studies have also been conducted recently. Boudreau, Dumas, Rahimpour and Oshkai (2018) carried out a water-tunnel experiment on this type of system at $Re \approx 2.1 \times 10^4$, and obtained a power coefficient of 0.86 and an efficiency of 31%. In addition, it was found that good performance can be attained over a wide range of flow and structural parameters, which is important from the practical point of view. A follow-up numerical study was then conducted on this system, which however obtained a much higher efficiency of 53.8% (Boudreau, Picard-Deland and Dumas, 2020). Using a NACA0015 foil at $Re \approx 6 \times 10^4$, Duarte, Dellinger, Dellinger, Ghenaim and Terfous (2019) studied the same type of system and found that the pivot axis should be located at least $0.29c$ from the leading edge to achieve continuous operation. They also revealed that the system can perform much better by increasing the heaving natural frequency.

In the fourth type, a group of heaving and pitching limiters are employed to help the foil achieve continuous flapping motions. Instead of utilizing the flutter instability, the foil is directly driven by hydrodynamic force/moment to flap along a guide rail and its linear and angular motions are constrained by a pair of heaving limiters and a pair of pitching limiters. This novel concept was firstly proposed by Platzer and colleagues (Platzer and Sarigul-Klijn, 2009; Platzer and Bradley, 2009). When successfully demonstrating the working principle of this concept, they also predicted the power extraction performance and pointed out potential applications. Recently, we experimentally studied the detailed fluid-structure interactions (FSI) of this concept and learnt the effects of several key parameters on the resulting power extraction performance (Mumtaz Qadri, Zhao and Tang, 2020). Our system can generate a mean power of about 1 W with an efficiency of 30.7%.

As a follow-up work, the present study aims to provide a useful guideline on the design and operation of our Type IV system through searching for the system's best performance. Both experimental and theoretical investigations are performed. In Section 2, the design and working principle of this Type IV system are briefly introduced, which is followed by the introduction of the measurement technologies and performance evaluation formulations in Section 3. The experimental results of a baseline case, an additional parametric study, and a search for the best performance are presented in Section 4. Then, a quasi-steady theoretical model for the system is developed, with which the system's performance is further explored in Section 5. This work is finally concluded with a useful guideline proposed on the design and operation of the system in Section 6.

2. Design and working principle

Although the design and working principle of our Type IV flapping-foil based flow-energy harvester have been introduced in details in Mumtaz Qadri et al. (2020), they are briefly described here for the sake of easy reference. As shown in Fig. 1, a rigid flat foil of 140-mm chord, 200-mm span, and 5-mm thickness is vertically installed on a T-shape platform through a long shaft and bearings. When immersed in water flow and subject to sufficient hydrodynamic forces/torques, the foil will undergo both heaving and pitching motions. Driven by the foil through the long shaft, however, the upper T-shape platform can only do purely translating motions along two linear guides.

To enable continuous heaving and pitching motions for the foil, two pairs of motion limiters are employed. As shown in Fig. 1(b), a pair of limiters are installed underneath the upstream linear guide, each consisting of an aluminum bar extruding towards the upstream. During the operation of the foil, these limiters periodically contact with a long heaving arm fixed on the pivot shaft of the foil, forcing the foil to rotate and reverse its stroke. In this way they refrain the foil's heaving amplitude, hence are termed "heaving limiters". The other pair of limiters are installed near the pivot shaft on the top of the upper T-shape platform. They periodically make contacts with a short pitching arm installed on the pivot shaft to refrain the foil's pitching amplitude, hence termed "pitching limiters". Both the heaving and pitching limiter pairs are designed in such a way that their locations are adjustable, so that the performance of the flow-energy harvester can be studied with pre-defined heaving and pitching amplitudes.

With the implementation of the motion limiters, the foil can achieve continuous flapping motions in water flow, hence extracting energy from the flow. The foil's kinematics can be generally divided into two phases, i.e., the "pure-heaving phase" and the "stroke-reversal phase". As depicted in Fig. 2, after its stroke reversal at the bottom side, the foil touches one of the pitching limiters at Instant 1, reaching and maintaining its maximum pitching angle at θ_0. With such a large pitching angle, the resulting hydrodynamic force pushes the foil upward until it touches the upper heaving limiter at Instant 3. This defines the pure-heaving phase as sketched in Fig. 2(a). When touching the upper heaving limiter, the foil is forced to rotate anticlockwise by the upper heaving limiter, reducing its pitching angle. As a result, the foil leaves the confining pitching limiter and enters the stroke-reversal phase. In the stroke-reversal phase, the foil
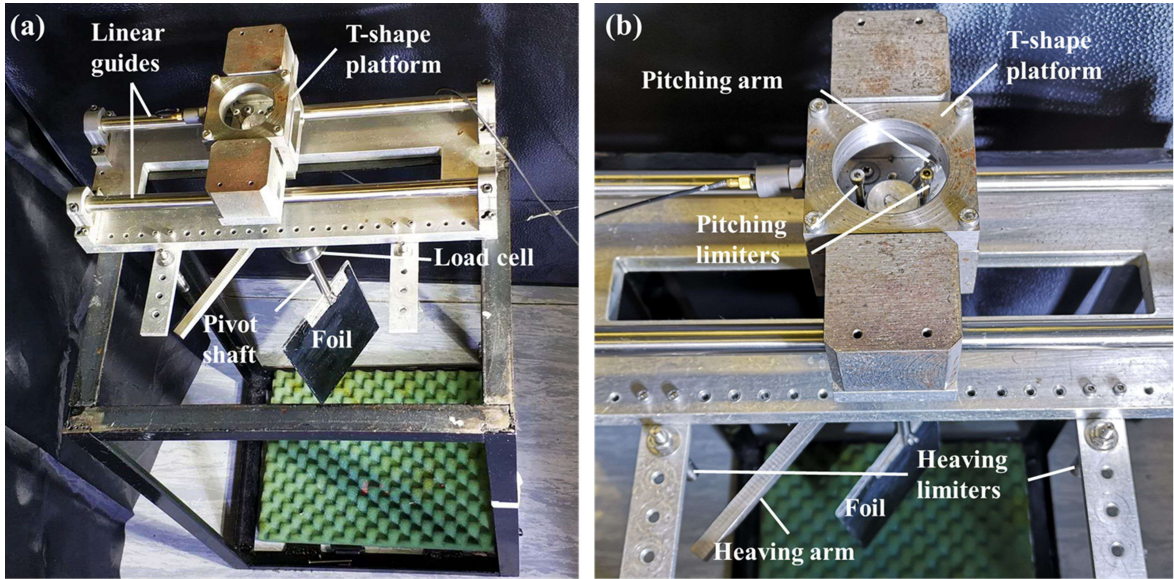
Figure 1: Test model for flow-energy harvesting using a fully passive flapping foil. The foil achieves continuous flapping motion using a pair of heaving limiters and a pair of pitching limiters.
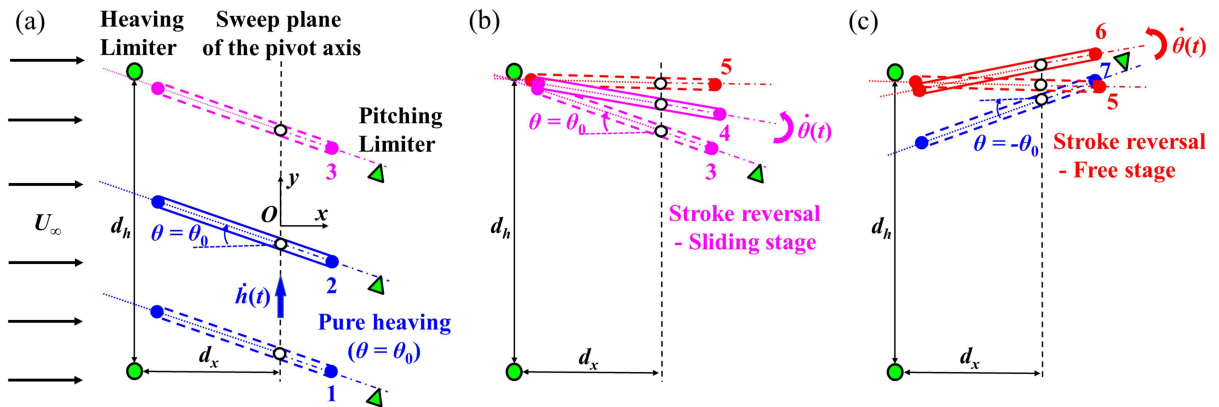
Figure 2: Schematics showing typical kinematics of the flapping foil in a half flapping cycle: (a) pure-heaving phase (in blue), (b) Sliding stage in stroke-reversal phase (in pink), (c) Free stage in stroke-reversal phase (in red). The numbers at the trailing edge indicate a time sequence of the foil's motion. Green circles represent heaving limiters, green triangles represent pitching limiters, and white circles represent the pivot axis. d_h is the the distance between the two heaving limiters, and d_x is the streamwise distance between the heaving limiters and the sweep plane of pivot axis. A ground-fixed coordinate system, Oxy, is defined in (a).

keeps rotating from $+\theta_0$ to $-\theta_0$ until it touches the other pitching limiter to start the next pure-heaving phase. Since the same pure-heaving and stroke-reversal phases will repeat during the subsequent downstroke, a complete flapping cycle consists of two pure-heaving phases and two stroke-reversal phases.

To facilitate the derivation of the theoretical model that is introduced in Appendix, the stroke-reversal phase is further divided into two stages. Take the upward-to-downward stroke reversal as an example. In the first stage, the foil keeps contacting with the upper heaving limiter and rotating due to the momentum gained in the preceding pure-heaving phase (represented by Instant 4). Note that, in this stage since the foil rotates together with its pivot shaft that moves vertical up along a straight line, the long heaving arm attached on the shaft has to slide on the heaving limiter. As such, the first stage is also called the "sliding stage", as sketched in Fig. 2(b). This stage ends at Instant 5 when the foil starts to leave the heaving limiter due to the reversed heaving force and pitching moment. After that, the foil

continues rotating anticlockwise (represented by Instant 6) until it touches the other pitching limiter and its pitching angle reaches $-\theta_0$ at Instant 7. This defines the second stage, or the "free stage", in which the foil has no contact with any limiter (represented by Instant 6).

3. Measurement and performance assessment

This flow-energy harvester was tested in a closed-circuit water channel. To eliminate the three-dimensional effect in the flow near the foil tips, a set of acrylic end plates were deployed along the upper and lower edges of the foil with a small clearance of approximately 3.5 mm. A high-speed camera (Photron Mini UX100) operating at 125 fps was used underneath the water channel to capture the foil's motions. A six-component load cell (ATI Mini-40) was used to measure the forces/torques experienced by the foil with a sampling rate of 2000 Hz, which was installed on the pivot shaft and located between the foil and the upper T-shape platform, as shown in Fig. 1 (a). The camera and the load cell were synchronized using a LabVIEW virtual instrument through a DAQ chassis (NI cDAQ 9174). More details about the measurements can be found in Mumtaz Qadri et al. (2020).

Note that, like all the existing studies listed in Table 1, the present flow-energy harvester only converts the flow kinetic energy into the foil system's mechanical energy and does not further convert the latter to electric energy by utilizing any power take-off system. Hence in this study the harvester's energy extraction performance was analyzed and evaluated based on the energy transfer from the flow kinetic energy to the foil system's mechanical energy.

The power extraction by the flapping foil, P, consists of two components: the power conversion by the heaving motion, P_h, and, the power conversion by the pitching motion, P_θ,

$$P = P_h + P_\theta = F_h \dot{h} + M_\theta \dot{\theta} \tag{1}$$

where F_h and M_θ are the transverse hydrodynamic force and the hydrodynamic pitching moment, respectively. $\dot{h}$ and $\dot{\theta}$ are the foil's heaving velocity and pitching velocity, respectively. Nondimensionalizing these powers using the foil and water flow properties gives the corresponding power coefficients

$$C_p = C_{ph} + C_{p\theta} = \frac{F_h \dot{h}}{\rho U_\infty^3 bc/2} + \frac{M_\theta \dot{\theta}}{\rho U_\infty^3 bc/2} = C_h \frac{\dot{h}}{U_\infty} + C_\theta \frac{\dot{\theta} c}{U_\infty} \tag{2}$$

where C_p is the total power coefficient, the summation of C_{ph}, the heaving power coefficient, and $C_{p\theta}$, the pitching power coefficient. C_h and C_θ are the coefficients for heaving force and pitching moment, respectively. ρ is the water density, U_∞ is the incoming flow velocity, and b and c are the foil's span and chord, respectively.

To assess the system's overall performance, the mean power coefficient can be evaluated as

$$\overline{C}_p = \frac{1}{T} \int_t^{t+T} C_p dt = \overline{C}_{ph} + \overline{C}_{p\theta} \tag{3}$$

where T is the foil's flapping period. $\overline{C}_{ph}$ and $\overline{C}_{p\theta}$ are the mean heaving and pitching power coefficients, respectively. The overall efficiency of the energy harvesting is then defined as the ratio of this mean power to the power carried in the incoming flow through the frontal area of the foil, i.e.,

$$\eta = \frac{\overline{P}}{\rho U_\infty^3 bh_0} = \frac{c}{2h_0} \overline{C}_p \tag{4}$$

where $\overline{P}$ is the time-averaged power, and h_0 is the foil's heaving amplitude defined as a half of the sweep distance of the pivot shaft. Note that, by using this definition, the obtained efficiency is generally larger than those calculated based on the foil's largest distance swept by the leading/trailing edge, the latter being normally used in literature as listed in Table 1.

4. Experimental results

4.1. A baseline case

A baseline case is chosen to show typical dynamics of the harvester, where the foil's pivot axis (i.e., the long pivot shaft) is located at $x_p = 0.7c$, the pitching amplitude is set as $\theta_0 = 30°$, and the water speed is set as $U_\infty = 0.55$ m/s
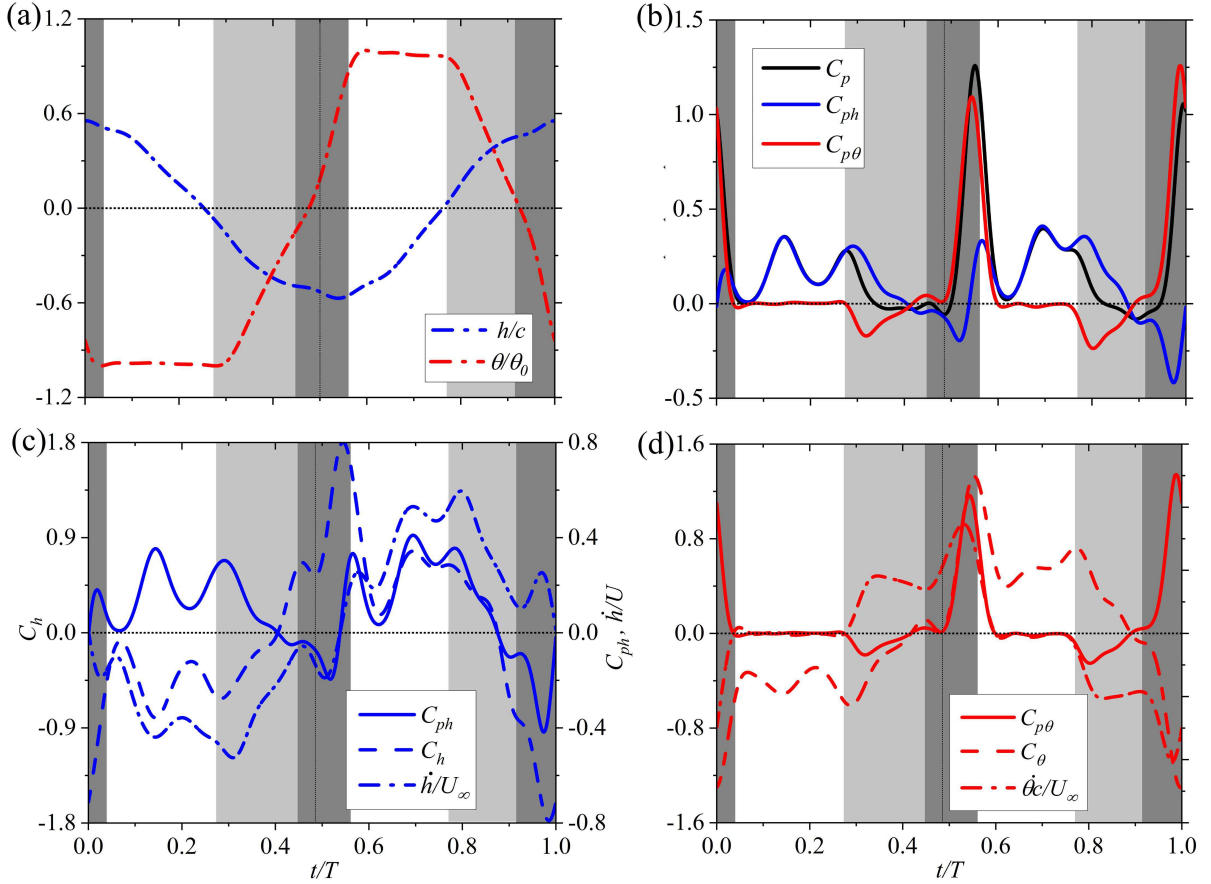
Figure 3: Evolution of the flapping foil's (a) heaving and pitching displacements, (b) power coefficients, (c) heaving velocity, force and power, and (d) pitching velocity, moment and power in a flapping cycle for the baseline case, where $U_\infty = 0.55$ m/s, $x_p = 0.7c$, $\theta_0 = 30°$, $d_h = 1.21c$ and $d_x = 0.75c$. All quantities are nondimensionalized. Throughout this work, the blue and red colors represent heaving and pitching related quantities, respectively, whereas the black color represents quantities associated with total performance. The white, light grey and dark grey backgrounds indicate the pure-heaving phase, the sliding stage, and the free stage, respectively.

(equivalent to the chord-based Reynolds number $Re = 7.7 \times 10^4$). Compared to the baseline case in Mumtaz Qadri et al. (2020), this baseline case adopts a smaller pitching amplitude (i.e., $\theta_0 = 30°$ v.s. $45°$), which is mainly for facilitating the parametric study on d_h in Section 4.2. A video showing the foil's continuous flapping motion can be found in the supplementary material (Video 1). Evolution of the heaving displacement and pitching angle in one flapping cycle is presented in Fig. 3(a), where $t/T = 0$ is defined as the instant when the pivot axis reaches its positive maximum. It is seen that the foil undergoes downstroke from $t/T = 0$ to 0.53 and then upstroke from $t/T = 0.53$ to 1, not strictly symmetric in time. The foil's pitching motion is not symmetric either. This observed asymmetry is attributed to the imperfect manufacturing and assembly of the test model.

In Fig. 3(a), the two pure-heaving phases are indicated with white background, where the pitching angle is maintained at either $+\theta_0$ or $-\theta_0$, whereas the two stroke-reversal phases are shaded in grey. It is clearly seen that the foil still undergoes significant heaving motion during stroke reversals, due to the non-zero streamwise distance between the foil's pivot axis and the two heaving limiters. Moreover, in each stroke-reversal phase, the sliding stage is shaded in light grey and the free stage in dark grey. These background settings are applied throughout this work to help discussions.

The power extraction performance of this flapping foil can be read from Fig. 3(b). It is seen that the total power (C_p) is positive in most of the time. It is dominated by the heaving motion in the pure-heaving phases and by the pitching motion in the free stage of stroke-reversal phases, but a competing result of these two in the sliding stage

Table 2
Time-averaged performance of the foil system in the baseline case

$\overline{C}_{ph}$	$\overline{C}_{p\theta}$	$\overline{C}_p = \overline{C}_{ph} + \overline{C}_{p\theta}$	$\overline{P}$ (W)	$\eta(\%)$
0.11	0.09	0.20	0.47	17.6

leading to slight power consumption. The time-averaged performance summarized in Table 2 further reveals that the contributions from these two motions are positive and also comparable, i.e., about 55% from the heaving motion and 45% from the pitching motion. The foil system generates a mean power of $\overline{P} = 0.47$ W, leading to a power extraction efficiency of $\eta = 17.6\%$.

The power extraction processes through the heaving and pitching motions are further presented in Figs. 3(c) and (d), respectively. It is observed from Fig. 3(c) that the foil's heaving velocity $\dot{h}/U_\infty$ reaches its extremes roughly at the end of each pure-heaving phase, while the heaving force C_h reaches its extremes roughly at the start of each pure-heaving phase, leading a phase difference of about 90°. As a result, the heaving power C_{ph} is positive in the pure-heaving phases but gradually becomes negative in the stroke-reversal phases especially in the free stage. As shown in Fig. 3(d), the pitching power $C_{p\theta}$ remains zero during the pure-heaving phases because of zero pitching velocity. It is negative in the sliding stages due to the out-of-phase relation between the pitching velocity $\dot{\theta}c/U_\infty$ and the pitching moment C_θ, but then shows a significant peak at the end of stroke reversals because both quantities peak there. More detailed discussions about the relations among the foil's kinematics, the hydrodynamic forces, the surrounding fluid flow, and the resulting power extraction can be found in Mumtaz Qadri et al. (2020).

4.2. Effects of d_h and d_x

In Mumtaz Qadri et al. (2020), we have investigated the effects of pivot location x_p, pitching amplitude θ_0, and water speed U_∞ (equivalently the Reynolds number Re). That is, as x_p increases, i.e., the foil's pivot axis moving towards the trailing edge, both the mean heaving power and the mean pitching power increase, so does the total power. The same trend was also observed when θ_0 increases from 30° to 60°. On the contrary, there exists an optimal U_∞ between 0.46 and 0.69 m/s, at which the power extraction efficiency is maximum. In the experiments, we also noticed that the distance between the two heaving limiters, d_h, and the streamwise distance between the heaving limiters and the sweep plane of pivot axis, d_x, play important roles in the foil system's dynamics. Hence, we study their effects in this subsection.

To study the effect of d_h, we vary it in the range from $0.79c$ to $1.43c$, covering the baseline case where $d_h = 1.21c$, while fixing all the other parameters. As revealed in Fig. 4(a), both the mean heaving power $\overline{C}_{ph}$ and the mean pitching power $\overline{C}_{p\theta}$ increase with d_h, so does the total power $\overline{C}_p$. However, the power extraction efficiency drops from $\eta = 22.4\%$ to 15.1%. These contrary trends are not surprising, because the increase in d_h also results in the increase in the sweep distance of the pivot axis, i.e., $2h_0$, such that the input power carried by the incoming flow as defined in the denominator of Eq. 4 also increases accordingly. Instead, these contrary trends indicate that, in the current d_h range, the gain of the power extraction due to the increase of d_h cannot compensate for the rise of unused input power.

Close inspection on the evolution of heaving and pitching quantities further reveals the causes for the increase of $\overline{C}_{ph}$ and $\overline{C}_{p\theta}$. As shown in Fig. 5(a), the increase of d_h increases the length of pure-heaving phases in the flapping cycle, or, in another word, reduces the length of stroke-reversal phases. This helps the heaving motion extract more power that mainly occurs during the heaving phases, as confirmed in Fig. 5(c), which explains the increase of $\overline{C}_{ph}$. As for the pitching motion, a shorter stroke-reversal phase indicates a faster pitching, promoting the power extraction at the end of the free stages, as revealed in Fig. 5(d). Meanwhile, the shortening of the sliding stages reduces the pitching-motion induced energy consumption. Collaboratively, these two factors cause the enhancement of $\overline{C}_{p\theta}$.

To study the effect of d_x, we vary it in the range from $0.61c$ to $0.89c$, covering the baseline case where $d_x = 0.75c$, while fixing all the other parameters. Fig. 4(b) reveals that, as d_x increases, the mean heaving power $\overline{C}_{ph}$ reduces, while the mean pitching power $\overline{C}_{p\theta}$ increases. Competition between these two leads to a decreasing trend for the total power $\overline{C}_p$. Since the change of d_x has very little effect on the input flow, the power extraction efficiency also follows the $\overline{C}_p$ trend, slightly dropping from $\eta = 18.9\%$ to 17.1%.

The evolution of the heaving and pitching displacements shown in Fig. 6(a) reveals that, as d_x increases, the length
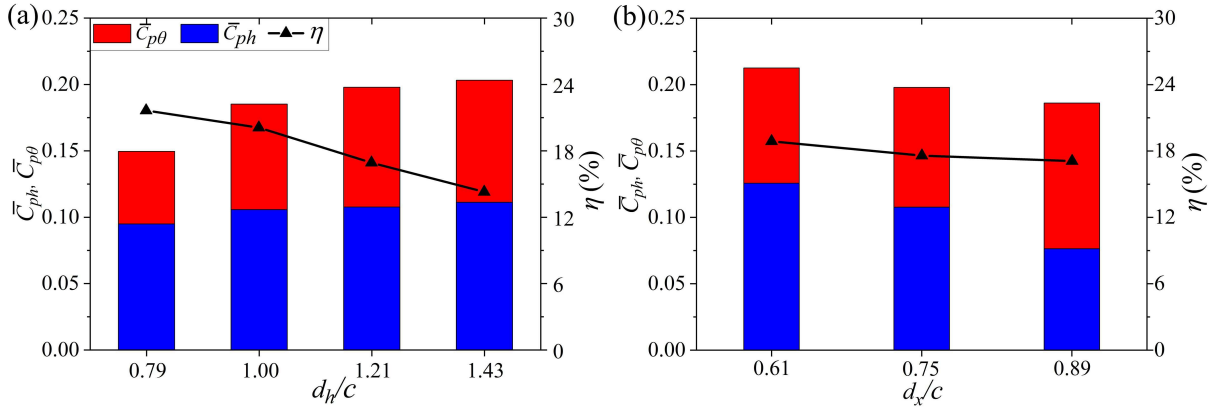
Figure 4: Variation of mean heaving, pitching and total power coefficients as well as power extraction efficiency against (a) the heaving limiter distance d_h and (b) the heaving-limiter-to-pivot-axis streamwise distance d_x. The other parameters are set the same as in the baseline case, i.e., $U_\infty = 0.55$ m/s, $x_p = 0.7c$, and $\theta_0 = 30°$.

of pure-heaving phases reduces, whereas the length of stroke-reversal phases increases. The shortened pure-heaving phase results in a smaller heaving velocity at the end of pure-heaving phase, which on one hand leads to degraded performance in heaving power extraction in the first half of the sliding stage, as shown in Fig. 6(c), and on the other hand leads to a smaller pitching power consumption in the same period, as shown in Fig. 6(d). This explains the decrease of $\overline{C}_{ph}$ and the increase of $\overline{C}_{p\theta}$ revealed in Fig. 4(b).

4.3. A search for the best performance

The results presented in Section 4.2 suggest that we can enhance the power extraction efficiency of the foil system, η, by adopting small d_h and d_x. This finding along with our previous ones in Mumtaz Qadri et al. (2020) give a clear guideline on finding the system's best power extraction performance. To facilitate the search, we adopt $d_h = 0.79c$ and $d_x = 0.61c$, both the smallest possible values in our experiments, and $x_p = 0.8c$, the farthest possible location for the foil's pivot axis from its leading edge. In addition, we vary the pitching amplitude from $\theta_0 = 15°$ to $60°$ and the water speed from $U_\infty = 0.52$ to 0.71 m/s, corresponding to the Reynolds number $Re = 7.3 \sim 9.9 \times 10^4$. Note that, the selection of U_∞ is constrained by the cut-in speed of 0.45 m/s for the foil system and the concern on structural integrity at high speeds.

The mean power coefficients and efficiencies of the foil system at different θ_0 and U_∞ are summarized in Fig. 7. It is seen that the foil system can achieve continuous operation only when U_∞ is sufficiently high. At low U_∞, such as 0.52 and 0.55 m/s, the system works only at moderate θ_0, i.e., 30° or 45°. This is because, at low U_∞ and small θ_0, the heaving force is small according to the lift theory, so that the system cannot accumulate enough momentum to overcome the dead center (i.e., $\theta_0 \approx 0°$), at which the hydrodynamic force/moment reverse the directions, and complete the stroke reversal. At low U_∞ and large θ_0, on the other hand, the pure-heaving phases are significantly shortened due to the geometric constraint, hence the system still cannot get enough momentum to complete the extended stroke reversals.

It is also seen from Fig. 7 that, at given U_∞, the mean heaving power $\overline{C}_{ph}$ increases with θ_0 in the current θ_0 range, mainly caused by the increase in the foil's angle of attack and hence the increase in both heaving force and heaving velocity. The mean pitching power $\overline{C}_{p\theta}$ also increases until reaching a peak at $\theta_0 = 45°$, a consequence of trade-off between the enhanced power consumption in the sliding stage and the enhanced power extraction at the end of the free stage. As a summation of these two, the total power $\overline{C}_p$ seems to peak between $\theta_0 = 45°$ and 60°. As for the power conversion efficiency, it generally follows the similar trend as that for $\overline{C}_p$, reaching maximum values of over $\eta = 40\%$ at either $\theta_0 = 45°$ or 60°. If observed from another perspective, at given θ_0, $\overline{C}_p$ and η generally do not vary too much with U_∞, probably due to the small U_∞ range adopted in the present study, except in some marginal cases where the foil system performs poorly or does not work at all.

Note that, the overall maximum efficiency of 42.7% (32.4% if evaluated using the swept distance of the foil's trailing edge) is obtained at $U_\infty = 0.71$ m/s and $\theta_0 = 60°$, the corresponding mean power output is about 1.51 W ($\overline{C}_p = 0.31$).
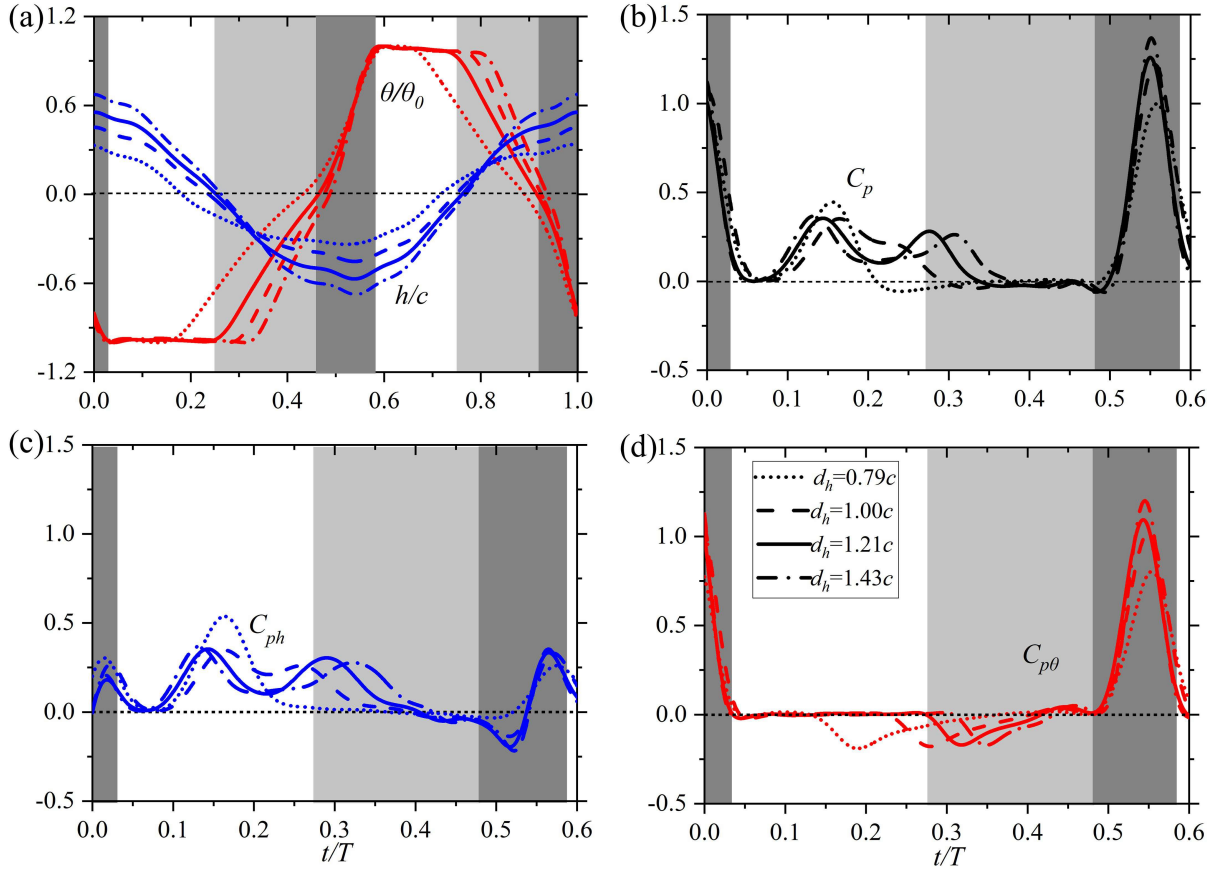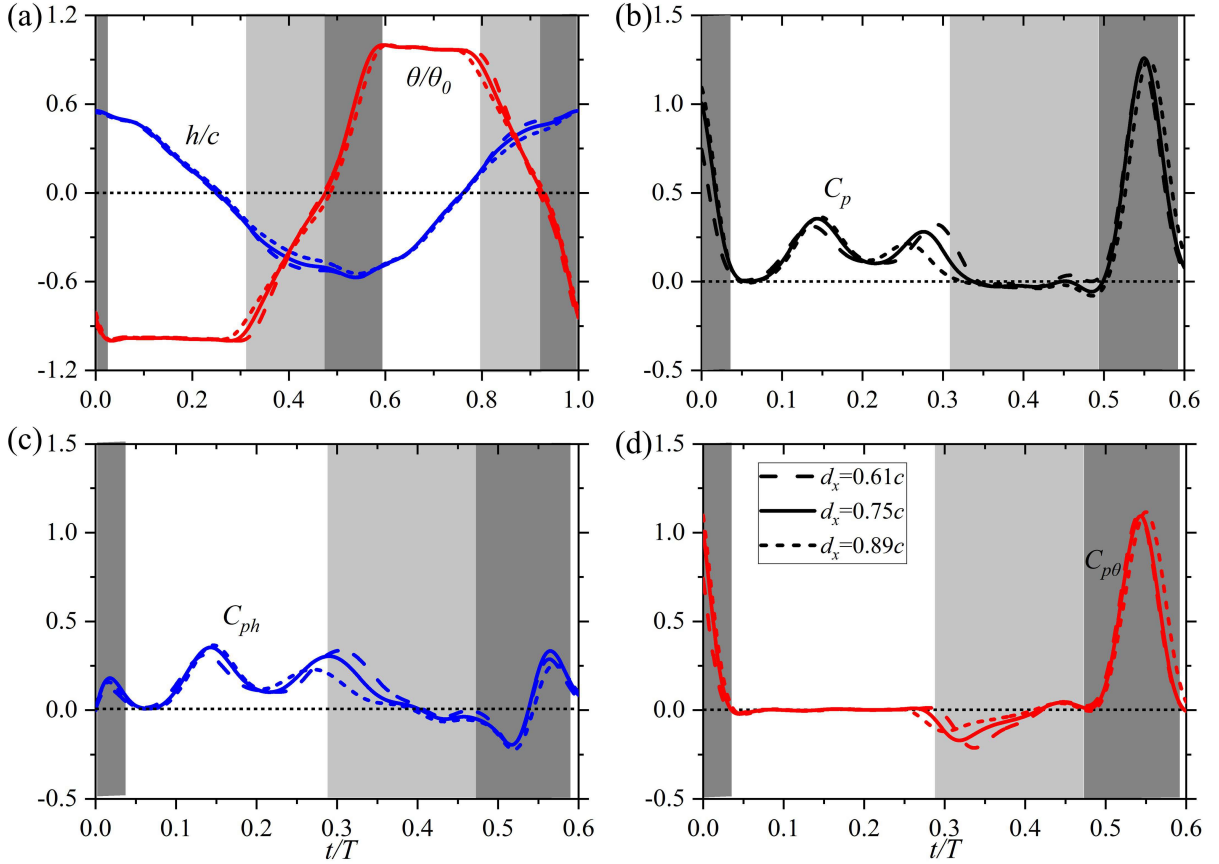
Figure 5: Comparison of the evolution of (a) heaving and pitching displacements, (b-d) total, heaving and pitching power coefficients, respectively, of the flapping foil with different heaving limiter distances. For better comparison, only the power curves in the downstroke are presented. Except d_h, all the other parameters are fixed at those in the baseline case, i.e., $U_\infty = 0.55$ m/s, $x_p = 0.7c$, $\theta_0 = 30°$ and $d_x = 0.75c$. The white, light grey and dark grey backgrounds indicate the pure-heaving phase, the sliding stage, and the free stage, respectively, in the baseline case where $d_h = 1.21c$.

Close inspection reveals that this case has quite different dynamics from that in the baseline case. As depicted by the evolution of displacements in Fig. 8(a), the pure-heaving phases disappear in this case, meaning that the foil never touches the pitching limiters during its flapping motions, as confirmed by the fact $\max(|\theta/\theta_0|) < 1$. Instead, the two stroke-reversal phases are directly connected to each other, and the system can smoothly operate with only a couple of heaving limiters (see Video 2 in the supplementary material). By comparing the power curves in Figs. 3(b) and 8(b), it seems that the change in the foil's dynamics does not affect its power extraction too much. The pitching motion still consumes energy in the sliding stages and extracts energy in the free stages. Due to the disappearance of the pure-heaving phases, the heaving motion only extracts energy in the first half of the sliding stages and in the second half of the free stage. Under this circumstance, however, the heaving motion still makes a greater contribution (about 60%) to the total power.

5. Theoretical prediction

To further explore the guidelines on the design and operation of the foil system, we extend the study using a theoretical model, which, based on the quasi-steady assumption, can fast predict the system's dynamics and power extraction performance with reasonable accuracy. The derivation and validation of this model can be found in Appendix. Since our experimental results have revealed that, in the ranges of investigation, both the mean power $\overline{C}_P$ and efficiency η share similar and nearly monotonic trends against the pivot location x_p, the pitching amplitude θ_0, and the heaving-

Figure 6: Comparison of the evolution of (a) heaving and pitching displacements, (b-d) total, heaving and pitching power coefficients, respectively, of the flapping foil with different heaving-limiter-to-pivot-axis streamwise distances. For better comparison, only the power curves in the downstroke are presented. Except d_x, all the other parameters are fixed at those in the baseline case, i.e., $U_\infty = 0.55$ m/s, $x_p = 0.7c$, $\theta_0 = 30°$ and $d_h = 1.21c$. The white, light-grey and dark-grey backgrounds indicate the pure-heaving phase, the sliding stage, and the free stage, respectively, in the baseline case where $d_x = 0.75c$.

limiter-to-pivot-axis streamwise distance d_x, here we choose their boundary values that can help maximize the foil's performance, i.e., $x_p = 0.8c$, $\theta_0 = 60°$ and $d_x = 0.61c$. We also learnt from Section 4.2 that $\overline{C}_P$ and η exhibit opposite trends against the heaving limiter distance d_h. Hence we adopted an intermediate value, i.e., $d_h = c$, to pursue balanced performance enhancement.

To determine a suitable water speed, we vary it in the largest possible range of our test facility from $U_\infty = 0.45$ to 1.05 m/s, corresponding to $Re = 6.3 \sim 14.7 \times 10^4$. The model predictions shown in Fig. 9 reveal that both $\overline{C}_P$ and η do not vary too much in the range of investigation, consistent with our experimental observations in Section 4 and also in Mumtaz Qadri et al. (2020). That is, $\overline{C}_P$ varies only between 0.40 and 0.47, and η varies only between 39% and 45%, both reaching their respective peaks at about $U_\infty = 0.6$ m/s. Hence, in the following analysis we adopt this optimal water speed that corresponds to $Re = 8.4 \times 10^4$.

In all the above studies, we fixed the mass of the foil and associated rotating part at $m_1 = 1.3$ kg, the relevant moment of inertia at $I_1 = 2.8 \times 10^{-3}$ kg-m^2, and the mass of the translation-only T-shape platform at $m_2 = 3.4$ kg. Here with the developed theoretical model we take a further step to investigate the influences of these masses on the system performance. Since, for given foil geometries, I_1 and m_1 are dependent to each other, only the effects of m_1 and m_2 are studied here. As shown in Fig. 10(a), as m_1 increases (so does I_1) while keeping m_2 fixed, both $\overline{C}_P$ and η reduce. These decreasing trends are very mild, especially when the dimensionless mass $m_1/\rho abc$ is less than about 15, where a, b and c are the foil's thickness, span and chord, respectively, and hence abc is the volume of the foil. This
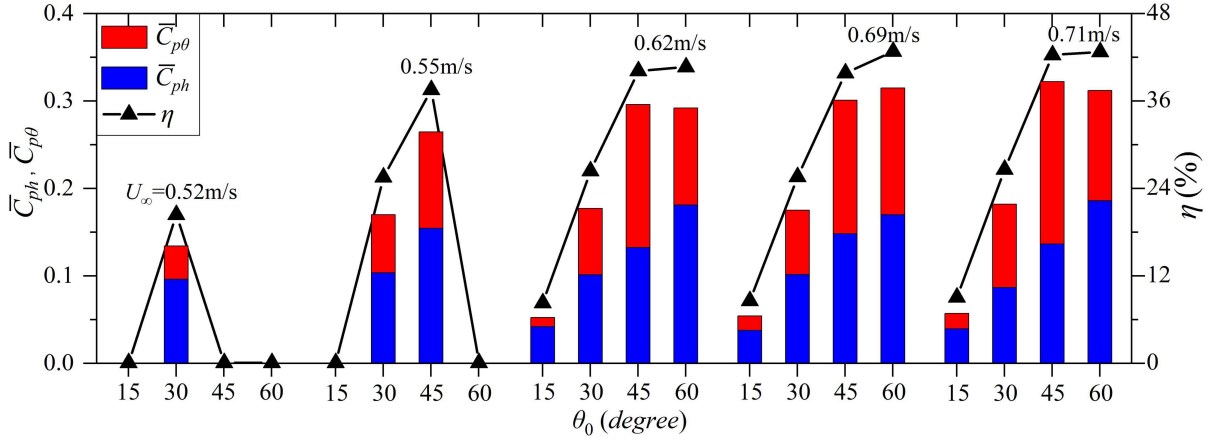
Figure 7: Variation of mean heaving, pitching and total power coefficients as well as power extraction efficiency against the heaving amplitude θ_0 and water speed U_∞. The other parameters are set as their respective optimal values, i.e., $x_p = 0.8c$, $d_h = 0.79c$ and $d_x = 0.61c$, in terms of power extraction efficiency.
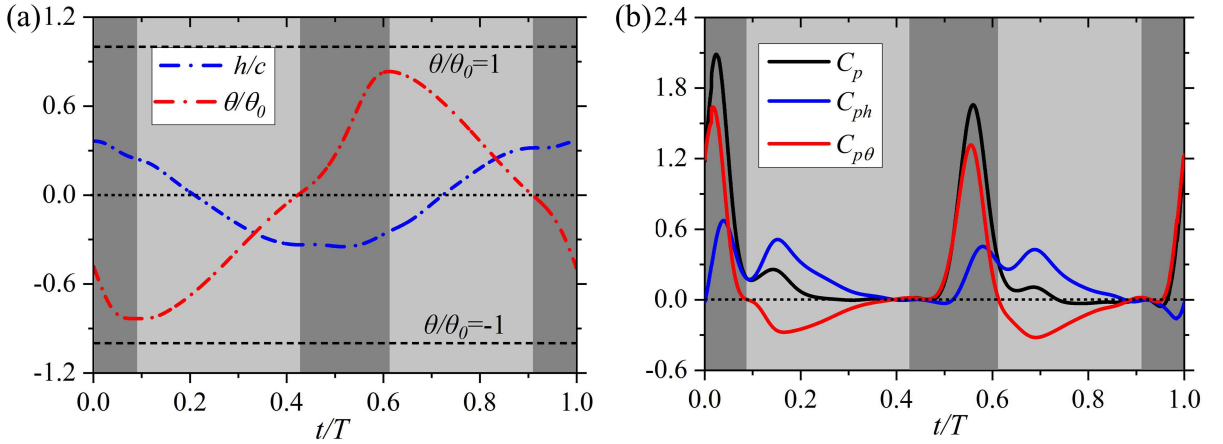

Figure 8: Evolution of the flapping foil's (a) heaving and pitching displacements and (b) power coefficients in the case that achieves the overall maximum efficiency of $43.x\%$, where $U_\infty = 0.71$ m/s, $x_p = 0.8c$, $\theta_0 = 60°$, $d_h = 0.79c$ and $d_x = 0.61c$. The dynamics of the foil's dynamics is quite different from the baseline case: the pure-heaving phases disappear, and a flapping cycle only includes two successive stroke-reversal phases. As such, only the light-grey and dark-grey backgrounds are presented.

observation is consistent with what has been reported in Boudreau et al. (2018), which is expected as a larger moment of inertia poses more challenges on stroke reversals. On the other hand, as m_2 increases while keeping m_1 fixed, both $\overline{C}_P$ and η increase first and then gradually decrease, leaving a peak at the dimensionless mass $m_2/\rho abc \approx 25$. This is reasonable because a very small translating mass can cause the reduction of the foil's effective angle of attack and the resulting hydrodynamic force/torque for power extraction, whereas a very large translating mass can result in very small heaving/pitching velocities, also leading to reduced power extraction. Note that, the currently used masses, i.e., $m_1/(\rho abc) = 9.4$ and $m_2/(\rho abc) = 24.3$, are already close to the optimum values.

If varying both d_h and θ_0 while fixing the other parameters, we obtain contours of $\overline{C}_p$ and η as shown in Fig. 11. A "no-pure-heaving" zone located at the upper left corner, i.e., small d_h and large θ_0, is well captured, in which the foil's pitching angle never reaches θ_0 and hence the system performance is independent of θ_0. In addition, in this zone $\overline{C}_p$ monotonically increases with d_h, while η shows a peak of 45% at around $d_h = c$. Outside this zone, $\overline{C}_p$ generally does not change with d_h except near the zone boundary, but increases with θ_0 in the current range of investigation. Hence the maximum $\overline{C}_p$ of 0.6 appears at the largest θ_0 as shown in Fig. 11(a), corresponding to a mean power of 1.8
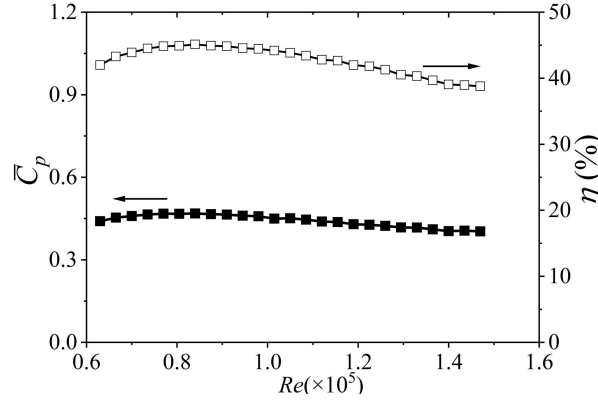
Figure 9: Variation of theoretically predicted mean total power coefficient and power extraction coefficient against the water speed. The other system parameters are chosen to pursue the enhancement of both $\overline{C}_p$ and η, i.e., $x_p = 0.8c$, $\theta_0 = 60°$, $d_x = 0.61c$ and $d_h = c$.
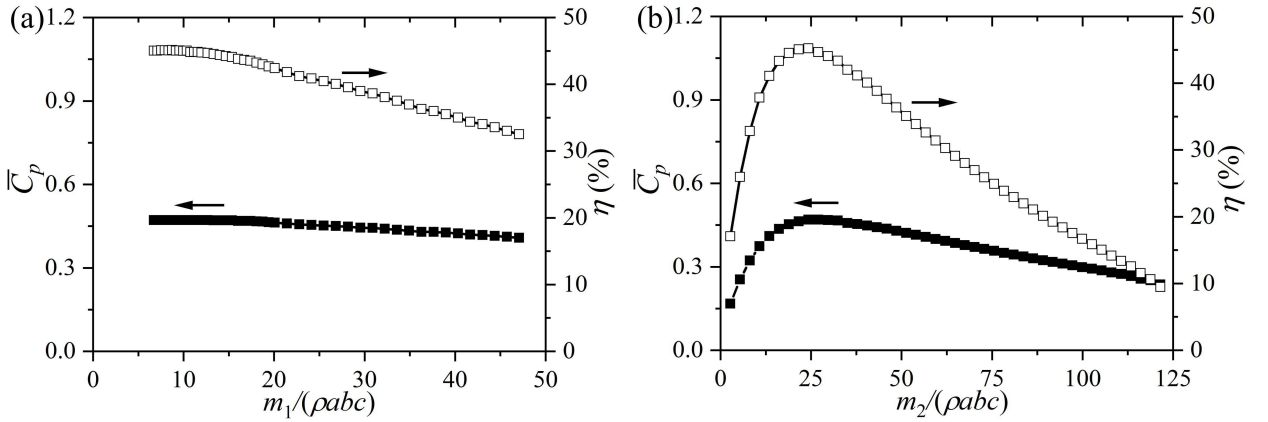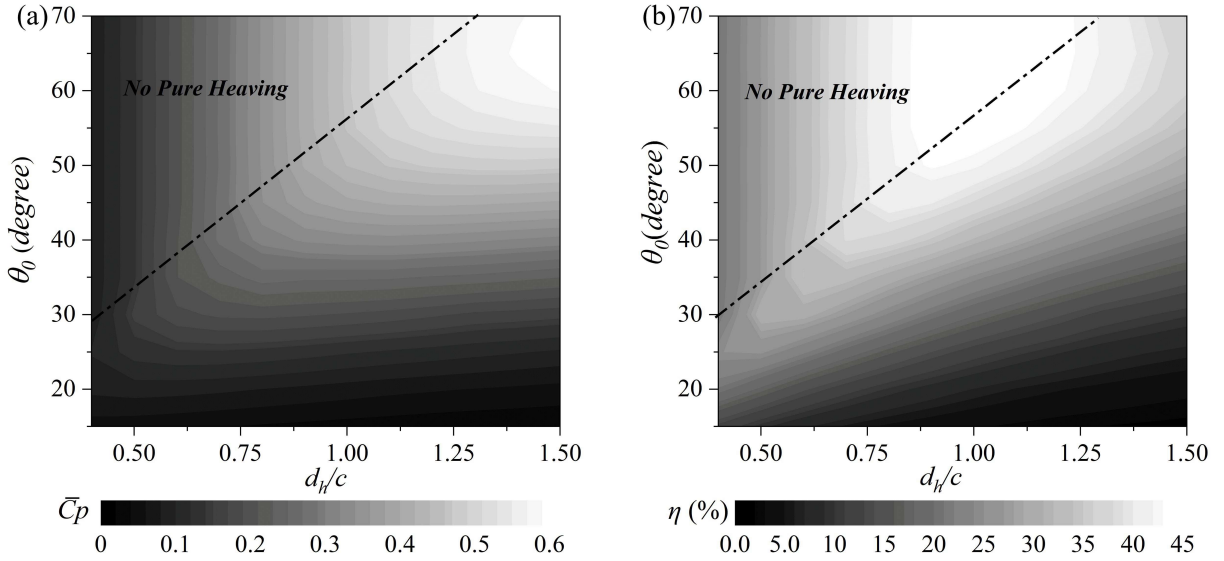

Figure 10: Variation of theoretically predicted mean total power coefficient and power extraction coefficient against (a) the mass of the foil and associated rotating part m_1 and (b) the mass of the translation-only T-shape platform m_2. The other system parameters are chosen to pursue the enhancement of both $\overline{C}_p$ and η, i.e., $U_\infty = 0.6$ m/s, $x_p = 0.8c$, $\theta_0 = 60°$, $d_x = 0.61c$ and $d_h = c$.

W. As for η, outside the no-pure-heaving zone it gradually reduces with d_h, but increases with θ_0. As such, its zonal maximum is located on the zone boundary. Collectively, the overall maximum $\overline{C}_p$ appears outside the no-pure-heaving zone at large θ_0 and d_h, while the overall maximum η appears in the zone at large θ_0 and intermediate d_h. Clearly, the maximum $\overline{C}_p$ and η do not occur under the same conditions.

6. Conclusions

We searched the best power extraction performance of a novel flow-energy harvester, which utilizes a flapping foil to extract energy from air/water flows without using any actuator. A series of water-tunnel experiments were conducted at $Re \approx 10^5$. Through investigating the effects of two key parameters, i.e., d_h and d_x, which were unexplored in our previous work (Mumtaz Qadri et al., 2020), a higher overall maximum efficiency of 42.7% was obtained at $U_\infty = 0.71$ m/s and $\theta_0 = 60°$, corresponding to a larger mean power output of about 1.51 W. A quasi-steady theoretical model was also developed to fast predict the system performance in a larger parameter space. The major findings are summarized as follows:

1. A no-pure-heaving zone is identified at small d_h and large θ_0. The overall maximum $\overline{C}_p$ appears at large d_h and large θ_0, outside but close to the zone boundary, whereas the overall maximum η appears at large θ_0 and

Figure 11: Contour of theoretically predicted (a) mean total power coefficient $\overline{C}_p$ and (b) power extraction efficiency η in the parametric map spanned by d_h and θ_0. A "no-pure-heaving" zone is identified at small d_h and large θ_0, where the foil system does not have the pure-heaving phase. The other system parameters are set as $U_\infty = 0.6$ m/s, $x_p = 0.8c$, and $d_x = 0.61c$.

      intermediate d_h, inside the no-pure-heaving zone.

2. The foil system can achieve continuous operations only when U_∞ is sufficiently high, reflecting the existence of a cut-in speed. Both $\overline{C}_p$ and η do not vary too much with U_∞, except in some marginal cases where the foil system performs poorly or does not work at all. However, optimum U_∞ does exist at which $\overline{C}_p$ and η reach their weak peaks.

3. Both $\overline{C}_p$ and η reduce with d_x and m_1, but show their peaks at intermediate m_2.

    The above findings together our previous findings in Mumtaz Qadri et al. (2020) suggest a useful guideline for enhancing the foil system's power extraction performance: large θ_0 and x_p, small d_x and m_1, and intermediate m_2 should be adopted. If the target is to increase the absolute power extraction, larger U_∞ and d_h are recommended. If the target is to enhance the power extraction efficiency, however, d_h close to the foil chord c is suggested. In the latter case, the system probably operates in the no-pure-heaving zone.

    Since our test model only converts the flow kinetic energy into the model's mechanical energy, in the near future we will complete the system by designing and deploying a suitable power take-off system and analyze the new system's water-to-wire power conversion performance.

A. A quasi-steady model

    We develop a quasi-steady theoretical model to fast predict the dynamics and power extraction performance of our fully passive flapping foil system. The model consists of a set of ordinary differential equations that describe the dynamics of the foil system in different phases/stages. In this model, the flapping foil is treated as a two-rigid-body system, and the hydrodynamic forces are evaluated based on the quasi-steady flow assumption, so that the lift theorem and steady force coefficients can be applied by ignoring the unsteady formation and shedding of vortices.

    Our fully passive flapping foil system is a two-rigid-body system, where one body undergoes both heaving and pitching motions, consisting of the foil, the long pivot shaft and the pitching arm for heaving limiter contacts, and the other body, i.e., the upper T-shape platform, experiences the heaving motion only. The free-body diagrams for both bodies in the pure-heaving phase, the sliding stage and the free stage are plotted in Fig. 12. In addition to the absolute coordinate system, Oxy (as defined in Fig. 2(a)), we define a foil-fixed coordinate system, $O'x'y'$, to help establish
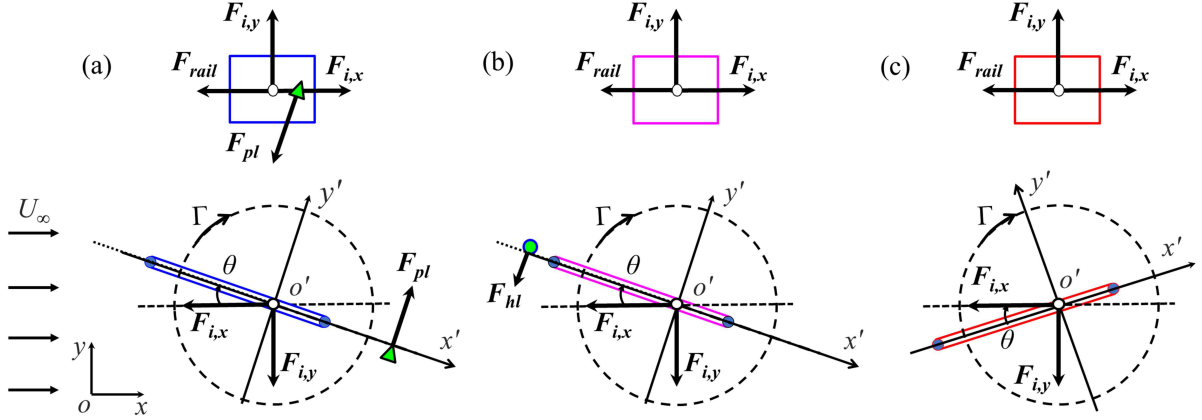
Figure 12: Free-body diagrams of the translating T-shape platform (top) and the flapping foil (bottom) in (a) the pure-heaving phase ($i = 1$), (b) the sliding stage ($i = 2$), and (c) the free stage ($i = 3$). The green circle represents the heaving limiter, the green triangle represents the pitching limiter, and white circles represent the pivot axis.

the governing equations, with its origin O' fixed at the pivot axis, x' axis pointing toward the foil's trailing edge, and y' axis perpendicular to the foil and pointing upward.

In the foil-fixed coordinate system, the velocity components of the foil's pivot axis relative to the freestream are

$$v_{x'} = -U_\infty \cos\theta - \dot{h}\sin\theta \tag{5}$$
$$v_{y'} = -U_\infty \sin\theta + \dot{h}\cos\theta \tag{6}$$

Hence applying the Newton's second law in this non-inertial reference frame to the rotatable part (mass m_1 and moment of inertia about the pivot axis I_1) gives

$$\left(m_1 + m_{x'x'}\right)\dot{v}_{x'} = -\left(m_1 + m_{y'y'}\right)\dot{\theta}v_{y'} + \rho\Gamma v_{y'} - F_{v,x'} - F_{i,x}\cos\theta + F_{i,y}\sin\theta \tag{7}$$

$$\left(m_1 + m_{y'y'}\right)\dot{v}_{y'} = \left(m_1 + m_{x'x'}\right)\dot{\theta}v_{x'} - \rho\Gamma v_{x'} - F_{v,y'} - F_{i,x}\sin\theta - F_{i,y}\cos\theta$$
$$+ \,\mathrm{sgn}\,(i-3)\left[\mathrm{sgn}\,(i-2)\,F_{pl} + \mathrm{sgn}\,(i-1)\,F_{hl}\right] \tag{8}$$

$$\left(I_1 + I_a\right)\ddot{\theta} = -m_{y'y'}\dot{v}_{y'}\left(x_p - \frac{c}{2}\right) - \rho\Gamma v_{x'}l_M - M_v$$
$$- \,\mathrm{sgn}\,(i-3)\left[\mathrm{sgn}\,(i-2)\,F_{pl}l_{pl} - \mathrm{sgn}\,(i-1)\,F_{hl}d_x\sec\theta\right] - c_\theta\dot{\theta} \tag{9}$$

where subscripts x, y, x' and y' indicate components along the respective axes. The Coriolis forces, $-m_1\dot{\theta}v_{y'}$ and $m_1\dot{\theta}v_{x'}$, arise due to the rotation of the $O'x'y'$ coordinate system. The terms $m_{x'x'}$, $m_{y'y'}$ and I_a are the foil's added mass/added moment of inertia, which can be evaluated from the inviscid-flow theory (Sedov, 1965)

$$m_{x'x'} = \frac{\pi}{4}\rho a^2 b, \qquad m_{y'y'} = \frac{\pi}{4}\rho c^2 b, \qquad I_a = \frac{\pi}{128}\left[1 + 32\left(\frac{x_p}{c} - \frac{1}{2}\right)^2\right]\rho\left(c^2 - a^2\right)^2 b \tag{10}$$

where a, b and c are the foil's thickness, span and chord, respectively. Since the foil's pivot axis is generally off the mid chord, I_a has been adjusted by applying the parallel axis theorem. In addition, the added mass force $m_{y'y'}\dot{v}_{y'}$ appearing in Eq. 9 is assumed to act at the mid chord and hence creates a moment arm of $x_p - c/2$ about the pivot axis (Bryant, Gomez and Garcia, 2013).

The lift experienced by the foil is orthogonal to the direction of motion and proportional to the circulation, Γ, which can be evaluated as (Wang, Birch and Dickinson, 2004; Andersen, Pesavento and Wang, 2005a)

$$\Gamma = C_T bc \frac{v_{x'}v_{y'}}{\sqrt{v_{x'}^2 + v_{y'}^2}} + \frac{1}{2}C_R bc^2\dot{\theta} \tag{11}$$

where $C_T = \pi$ in the first term that quantifies the contribution from the foil's translational motions, and $C_R = 1.0$ in the second term that describes the contribution from the foil's pitching motion. Since the point of application of the circulation-induced lift changes its location with the pitching angle, the moment arm of this lift relative to the pivot axis appearing in Eq. 9 can be evaluated as (Boccalero, Olivieri, Mazzino and Boragno, 2017)

$$l_M = x_p - \frac{c}{4}(2 - \cos\theta) \tag{12}$$

Another moment arm appearing in Eq. 9, $l_{pl} = 0.2c$, is the distance between the pitching limiter and the pivot axis.

In Eqs. 7 to 9, F_v and M_v are the drag and dissipative fluid moment, respectively, which can be determined as (Wang et al., 2004; Andersen et al., 2005a; Huang, Liu, Wang, Wu and Zhang, 2013)

$$F_v = \frac{1}{2}\rho bc\left[C_D(0)\frac{v_{x'}^2}{\sqrt{v_{x'}^2 + v_{y'}^2}} + C_D\left(\frac{\pi}{2}\right)\frac{v_{y'}^2}{\sqrt{v_{x'}^2 + v_{y'}^2}}\right](v_{x'}, v_{y'}) \tag{13}$$

$$M_v = \frac{1}{64}C_D\left(\frac{\pi}{2}\right)\rho bc^4|\dot\theta|\dot\theta \tag{14}$$

where $C_D(0) = 0.05$ and $C_D(\pi/2) = 1.6$ are the foil's drag coefficients at 0 and $\pi/2$ angles of attack, respectively, according to Bryant et al. (2013).

In Eqs. 7 to 9, F_i is the internal force between the rotatable part and the upper T-shape platform, which is resolved in the Oxy coordinate system. F_{pl} and F_{hl} are the contact forces from the pitching limiters and heaving limiters, respectively, which are perpendicular to their respective limiter arms under the no-friction assumption, i.e., along the y' axis. c_θ in Eq. 9 is the damping coefficient for pitching motion.

A number of sign functions are also applied in Eqs. 7 to 9, such that the foil's dynamics in both the pure-heaving and stroke-reversal phases (the latter further includes the sliding and free stages) can be described using just one set of equations. Here we define a switch variable i, i.e., $i = 1$ when Eqs. 7 to 9 describe the foil's dynamics in the pure-heaving phase, $i = 2$ in the sliding stage, and $i = 3$ in the free stage. In the pure-heaving phase, the pitching angle is fixed at θ_0 during the upstroke or $-\theta_0$ during the downstroke, i.e.,

$$\theta = \pm\theta_0, \qquad \text{as } i = 1 \tag{15}$$

In the sliding stage, the pitching arm is sliding over one of the pitching limiters, hence the foil's heaving velocity $\dot h$ and pitching velocity $\dot\theta$ are related geometrically as

$$\dot h = -d_x\dot\theta\sec^2\theta, \qquad \text{as } i = 2 \tag{16}$$

In the free stage, the foil is not in contact with any of the motion limiters. As such, there is no additional equation for $i = 3$.

Applying the Newton's second law in the absolute coordinate system to the T-shape platform (mass m_2) gives

$$m_2\ddot h = F_{i,y} - \text{sgn}(i-3)\,\text{sgn}(i-2)\,F_{pl}\cos\theta - c_h\dot h \tag{17}$$

where c_h is the damping coefficient for heaving motion.

To this end, there are in total eight unknowns in this dynamic system, i.e., $v_{x'}$, $v_{y'}$, $\dot h$, θ, $F_{i,x}$, $F_{i,y}$, F_{pl} and F_{hl}. Specifically, in the pure-heaving phase ($i = 1$), we need to determine seven out of the eight unknowns (except F_{hl}) by solving seven equations, i.e., Eqs. 5 to 9, 15 and 17. In the sliding stage ($i = 2$), we also need to determine seven unknowns (except F_{pl}) by solving seven equations, i.e., Eqs. 5 to 9, 16 and 17. As for the free stage ($i = 3$), we only need to determine six unknowns (except F_{hl} and F_{pl}) by solving six equations, i.e., Eqs. 5 to 9 and 17. As such, we can find closed-form solutions for this novel dynamic system. These sets of ordinary differential equations are then solved using the 4th-order Runge-Kutta method.

Once the solutions to the above systems of equations are obtained, the instantaneous hydrodynamic force/torque experienced by the foil can be calculated as

$$F_h = (m_1 + m_2)\ddot h + F_{hl}\cos\theta + c_h\dot h \tag{18}$$
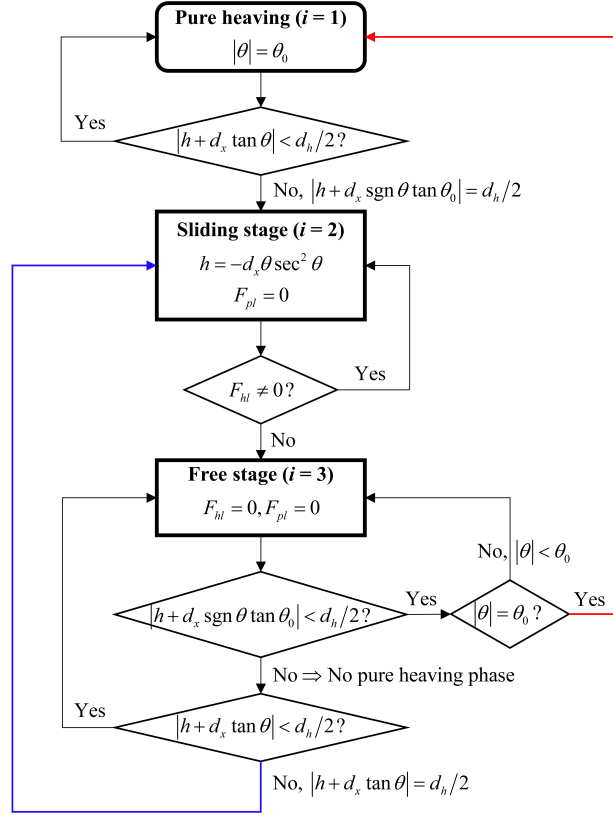
Figure 13: Flowchart showing the loops of evaluation and conditions of transition among different phases/stages. The red arrow indicates the loop for normal dynamics including both pure-heaving and stroke-reversal phases, whereas the blue arrow indicates the loop for no-pure-heaving dynamics.

$$M_\theta = I\ddot{\theta} + F_{pl}d_x \sec\theta + c_\theta\dot{\theta} \tag{19}$$

The foil's power extraction performance is then evaluated using Eqs. 1 to 4.

The transition among different phases/stages is depicted in the flowchart in Fig. 13. Whether the foil has reached the sliding stage from the pure-heaving phase depends on the relationship among the heaving displacement, h, and the other two distances, i.e., d_x and d_h. Geometrically, the transverse displacement of the heaving arm in the plane connecting the two heaving limiters is $h + d_x \tan\theta$, which falls in the range from $-d_h/2$ to $d_h/2$ since the heaving arm always moves between the two heaving limiters. Hence $|\theta| = \theta_0$ and $|h + d_x \tan\theta| < d_h/2$ during pure heaving. When the heaving arm touches one of the heaving limiters, $|h + d_x \tan\theta| = |h + d_x \text{sgn}\,\theta \tan\theta_0| = d_h/2$, which defines the end of pure heaving and the start of sliding stage. In the sliding stage, the heaving arm slides over the heaving limiter, generating non-zero contact force, i.e., $F_{hl} \neq 0$. Hence $F_{hl} = 0$ defines the end of sliding stage and the start of free stage.

Compared to the above two, the transition from the free stage is more complicated. We should first assess whether the preset pitching amplitude, θ_0, can be reached in this stage. This is done by checking, if pitched at θ_0 or $-\theta_0$, whether the heaving arm still moves between the two heaving limiters, i.e., $|h + d_x \text{sgn}\,\theta \tan\theta_0| < d_h/2$. If under this condition the foil's actual pitching angle reaches the preset amplitude, i.e., $|\theta| = \theta_0$, the free stage ends, followed by a new pure-heaving phase. However, if at some point the condition does not hold, the heaving arm will probably touch the opposite heaving limiter with a pitching angle $|\theta| < \theta_0$, which is also the actual maximum pitching angle throughout the entire flapping process. In this case, there will be no pure-heaving phase, and the free stage will be directly followed by a new sliding stage. Furthermore, the two pitching limiters are not actually in use and can be removed. This phenomenon has been well reported in Section 4.3 and presented in Video 2.

Note that, in addition to the quasi-steady assumption that involves C_T, C_R and C_D, derivation of the above model

---

Table 3
Comparison of model predictions and experimental data on the foil system's time-averaged performance

	Case A1: $U_\infty = 0.55$ m/s, $\theta_0 = 30°$, $x_p = 0.7c, d_h = 0.79c$, $d_x = 0.61c$					Case A2: $U_\infty = 0.62$ m/s, $\theta_0 = 60°$, $x_p = 0.8c, d_h = 0.79c$, $d_x = 0.61c$				
	$\overline{C}_{ph}$	$\overline{C}_{p\theta}$	$\overline{C}_p$	$\overline{P}$ (W)	$\eta(\%)$	$\overline{C}_{ph}$	$\overline{C}_{p\theta}$	$\overline{C}_p$	$\overline{P}$ (W)	$\eta(\%)$
Model	0.08	0.08	0.16	0.35	22.8	0.18	0.08	0.26	0.87	37.7
Experiment	0.09	0.06	0.15	0.33	22.3	0.18	0.11	0.29	0.97	40.6

involves several other simplifications and assumptions. First, the formation and shedding of vortices from the flapping foil are not taken into account, which may significantly affect the force/torque generation and the resulting dynamics. Second, the actual dimensions of all the heaving/pitching arms and limiters are not considered, which may affect the boundary definitions among different phases/stages. Third, the friction between the heaving arm and limiters during the sliding stage is ignored, which affects the evaluation of F_{hl}. Last, possible wall effects that are experienced in the experiments are not considered, which may affect the foil's dynamics when d_h is large. All these simplifications and assumptions could affect the model's validity and accuracy.

To validate this quasi-steady model, we compare its predicted results with our experimental data. In the simulation, we adopted the same parameter values as in the experiments, i.e., the thickness, span and chord of the foil $a = 5$ mm, $b = 200$ mm and $c = 140$ mm, the mass and moment of inertia of the foil and associated parts $m_1 = 1.3$ kg and $I_1 = 2.4 \times 10^{-3}$ kg-m^2 for $x_p = 0.7c$ ($I_1 = 2.8 \times 10^{-3}$ kg-m^2 for $x_p = 0.8c$), the mass of the T-shape platform $m_2 = 3.4$ kg, and water density $\rho = 1000$ kg/m^3. The damping coefficients for the having and pitching motions are evaluated as $c_h = 0.05$ N-s/m and $c_\theta = 0.1$ N-m-s, respectively.

Two cases are chosen for the comparison: one includes pure-heaving phases operating with $U_\infty = 0.55$ m/s, $\theta_0 = 30°$, $x_p = 0.7c$, $d_h = 0.79c$ and $d_x = 0.61c$ (denoted as Case A1), and the other does not include pure-heaving phases operating with $U_\infty = 0.62$ m/s, $\theta_0 = 60°$, $x_p = 0.8c$, $d_h = 0.79c$ and $d_x = 0.61c$ (denoted as Case A2). The comparison results in these two cases are presented in Figs. 14 and 15, respectively, which reveal that the model can predict the evolution of the foil system's dynamics and power extraction performance reasonably well. The curves representing the model predictions are generally smoother than those representing the experimental data, except some abrupt changes in pitching velocity and pitching power when transitions between different phases/stages occur. From these abrupt changes, it can be observed that, in Case A1, the model predicts much shorter pure-heaving phases and slightly longer free stages, whereas this phase/stage difference is not prominent in Case A2 where no pure heaving occurs.

The time-averaged performance is also compared in Table 3. It reveals that the predicted mean powers and efficiencies are fairly close to the experimental values in both cases, indicating that, despite many simplifications and assumptions, the present model can provide reasonable, fast predictions in the foil system's power extraction performance.

Acknowledgement

References

Andersen, A., Pesavento, U., Wang, Z.J., 2005a. Unsteady aerodynamics of fluttering and tumbling plates. J. Fluid Mech. 541, 65–90.

Boccalero, G., Olivieri, S., Mazzino, A., Boragno, C., 2017. Power harvesting by electromagnetic coupling from wind-induced limit cycle oscillations. Smart Mater. Struct. 26, 095031.

Boudreau, M., Dumas, G., Rahimpour, M., Oshkai, P., 2018. Experimental investigation of the energy extraction by a fully-passive flapping-foil hydrokinetic turbine prototype. J. Fluids Struct. 82, 446–472.

Boudreau, M., Picard-Deland, M., Dumas, G., 2020. A parametric study and optimization of the fully-passive flapping-foil turbine at high reynolds number. Renew. Energy 146, 1958–1975.

Bryant, M., Gomez, J.C., Garcia, E., 2013. Reduced-order aerodynamic modeling of flapping wing energy harvesting at low reynolds number. AIAA J. 51, 2771–2782.
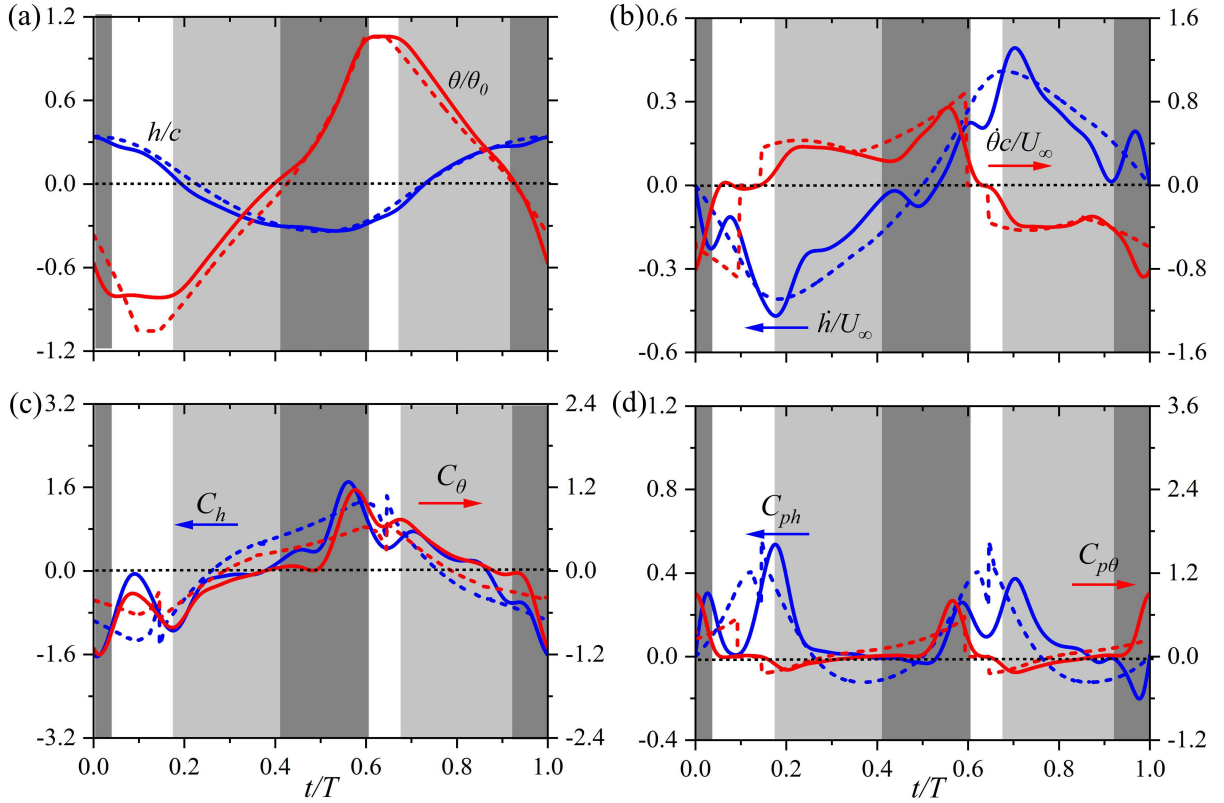
Figure 14: Comparison of predicted and actual evolution of the flapping foil's heaving and pitching (a) displacements, (b) velocities, (c) hforce/moment and (d) power in a flapping cycle for a case operating with pure-heaving phases, where $U_\infty = 0.55$ m/s, $x_p = 0.7c$, $\theta_0 = 30°$, $d_h = 0.79c$ and $d_x = 0.61c$. All quantities are nondimensionalized. The solid lines are from the experimental data and the dashed lines are from the theoretical predictions. The blue and red curves represent heaving and pitching related quantities, respectively. The white, light grey and dark grey backgrounds indicate the pure-heaving phase, the sliding stage, and the free stage, respectively, in the experiment.

Duarte, L., Dellinger, N., Dellinger, G., Ghenaim, A., Terfous, A., 2019. Experimental investigation of the dynamic behaviour of a fully passive flapping foil hydrokinetic turbine. J. Fluids Struct. 88, 1–12.

Huang, W., Liu, H., Wang, F., Wu, J., Zhang, H.P., 2013. Experimetal study of a freely falling plate with an inhomogeneous mass distribution. Phys. Rev. E 88, 053008.

Jiang, W., Wang, Y.L., Zhang, D., Xie, Y.H., 2019. Numerical investigation into power extraction by a fully passive oscillating foil with double generators. Renew. Energy 133, 32–43.

Jiang, W., Wang, Y.L., Zhang, D., Xie, Y.H., 2020. Numerical investigation into the energy extraction characteristics of 3d self-induced oscillating foil. Renew. Energy 148, 60–71.

Jones, K.D., Davids, S., Platzer, M.F., 1999. Oscillating-wing power generator, in: Proc. 3rd ASME/JSME Joint Fluids Eng. Conf., pp. FEDSM99–7050.

Jones, K.D., Lindsey, K., Platzer, M.F., 2003. An investigation of the fluid-structure interaction in an oscillating-wing micro-hydropower generator, in: WIT Transactions on The Built Environment, pp. 73–82.

Kim, D., Strom, B., Mandre, S., Breuer, K., 2017. Energy harvesting performance and flow structure of an oscillating hydrofoil with finite span. J. Fluids Struct. 70, 314–326.

Kinsey, T., Dumas, G., 2012a. Computational fluid dynamics analysis of a hydrokinetic turbine based on oscillating hydrofoils. J. Fluids Eng.-Trans. ASME 134, 021104.

Kinsey, T., Dumas, G., 2012b. Optimal tandem configuration for oscillating-foils hydrokinetic turbine. J. Fluids Eng.-Trans. ASME 134, 031103.

Kinsey, T., Dumas, G., Lalande, G., Ruel, J., Mehut, A., Viarouge, P., Lemay, J., Jean, Y., 2011. Prototype testing of a hydrokinetic turbine based on oscillating hydrofoils. Renew. Energy 36, 1710–1718.

Liu, Z., Qu, H., Shi, H., 2020. Energy-harvesting performance of a coupled-pitching hydrofoil under the semi-passive mode. Appl. Energy 267, 114889.

McKinney, W., DeLaurier, J., 1981. The wingmill: An oscillating-wing windmill. J. Energy 5, 109.

Mumtaz Qadri, M.N., Zhao, F., Tang, H., 2020. Fluid-structure interaction of a fully passive flapping foil for flow energy extraction. Int. J. Mech.
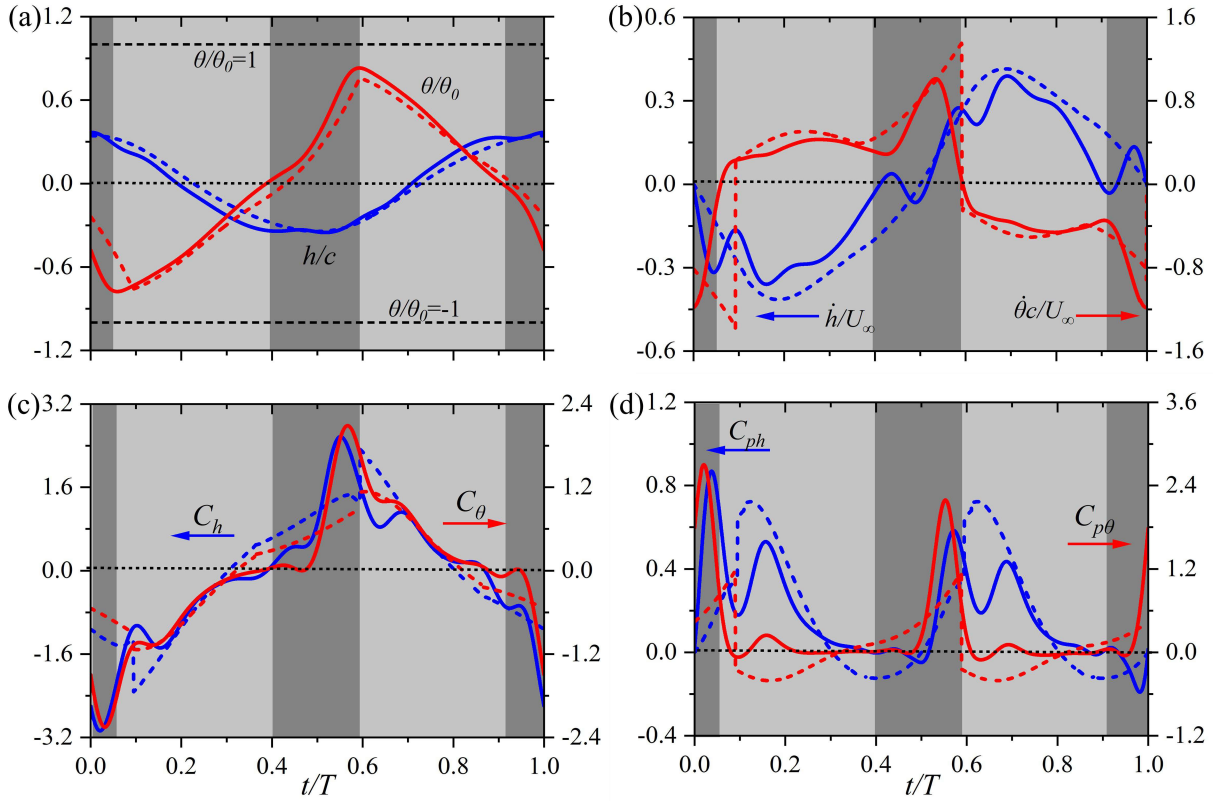
Figure 15: Comparison of predicted and actual evolution of the flapping foil's heaving and pitching (a) displacements, (b) velocities, (c) hforce/moment and (d) power in a flapping cycle for a case operating in the no-pure-heaving zone, where $U_\infty = 0.62$ m/s, $x_p = 0.8c$, $\theta_0 = 60°$, $d_h = 0.79c$ and $d_x = 0.61c$. All quantities are nondimensionalized. The solid lines are from the experimental data and the dashed lines are from the theoretical predictions. The blue and red curves represent heaving and pitching related quantities, respectively. The light- and dark-grey backgrounds indicate the sliding stage and the free stage, respectively, in the experiment.

Sci. 177, 105587.

Peng, Z., Zhu, Q., 2009. Energy harvesting through flow-induced oscillations of a foil. Phys. Fluids 21, 123602.

Platzer, M.F., Bradley, R.A., 2009. Oscillating-wing power generator with flow-induced pitch-plunge phasing. US Patent US20090121490A1.

Platzer, M.F., Sarigul-Klijn, N., 2009. A novel approach to extract power from free-flowing water and high altitude jet streams, in: Proc. of ASME 2009 3rd International Conference on Energy Sustainability, pp. ES2009–90146.

Sedov, L.I., 1965. Two-dimensional Problems in Hydrodynamics and Aerodynamics. John Wiley.

Veilleux, J., Dumas, G., 2017. Numerical optimization of a fully passive flapping airfoil turbine. J. Fluids Struct. 70, 102–130.

Wang, Z., Du, L., Zhao, J., Thompson, M.C., Sun, X., 2020. Flow-induced vibrations of a pitching and plunging airfoil. J. Fluid Mech. 885, A36.

Wang, Z.J., Birch, J.M., Dickinson, M.H., 2004. Unsteady forces and flows in low reynolds number hovering flight: two-dimensional computations vs robotic wing experiments. J. Exp. Biol. 207, 449–460.

Xiao, Q., Liao, W., Yang, S., Peng, Y., 2012. How motion trajectory affects energy extraction performance of a biomimic energy generator with an oscillating foil. Renew. Energy 37, 61–75.

Xiao, Q., Zhu, Q., 2014. A review on flow energy harvesters based on flapping foils. J. Fluids Struct. 46, 174–191.

Xu, W., Xu, G., Duan, W., Song, Z., Lei, J., 2019. Experimental and numerical study of a hydrokinetic turbine based on tandem flapping foils. Energy 174, 375–385.

Young, J., Ashraf, M.A., Lai, J.C.S., Platzer, M.F., 2013. Numerical simulation of fully passive flapping foil power generation. AIAA J. 51, 2727–2739.

Young, J., Lai, J.C., Platzer, M.F., 2014. A review of progress and challenges in flapping foil power generation. Prog. Aerosp. Sci. 67, 2–28.

Zhu, Q., 2011. Optimal frequency for flow energy harvesting of a flapping foil. J. Fluid Mech. 675, 495–517.